IEEE Access
Multidisciplinary ⋮ Rapid Review ⋮ Open Access Journal

Received November 12, 2018, accepted November 26, 2018, date of publication December 4, 2018,
date of current version December 31, 2018.

*Digital Object Identifier 10.1109/ACCESS.2018.2884704*

# Scatter Artifacts Removal Using Learning-Based Method for CBCT in IGRT System

**SHIPENG XIE[1], CHENGYUAN YANG[1], ZIJIAN ZHANG[2], AND HAIBO LI[1,3]**

[1]College of Telecommunications & Information Engineering, Nanjing University of Posts and Telecommunications, Nanjing 210003, China
[2]Department of Oncology, Xiangya Hospital Central South University, Changsha 410008, China
[3]Department of Media Technology and Interaction Design, School of Electrical Engineering and Computer Science, KTH Royal Institute of Technology, 10044 Stockholm, Sweden

Corresponding authors: Shipeng Xie (xie@njupt.edu.cn) and Haibo Li (lihb@njupt.edu.cn)

This work was supported by the University Natural Science Research Project of Jiangsu Province under Grant 17KJB510038.

**ABSTRACT** Cone-beam-computed tomography (CBCT) has shown enormous potential in recent years, but it is limited by severe scatter artifacts. This paper proposes a scatter-correction algorithm based on a deep convolutional neural network to reduce artifacts for CBCT in an image-guided radiation therapy (IGRT) system. A two-step registration method that is essential in our algorithm is implemented to preprocess data before training. The testing result on real data acquired from the IGRT system demonstrates the ability of our approach to learn artifacts distribution. Furthermore, the proposed method can be applied to enhance the performance on such applications as dose estimation and segmentation.

**INDEX TERMS** CBCT, scatter correction, image registration, deep CNN.

## I. INTRODUCTION

Cone-beam computed tomography (CBCT) system based on flat-panel detectors (FPDs) has shown enormous potential in the past two decades. Compared with traditional computed tomography (CT), CBCT has numerous advantages, such as higher spatial resolution, scanning speed and ray utilization ratio, lower radiation dose and effective solution to set-up errors of the patients treated with fractioned radiotherapy [1]. However, one major challenge encountered by CBCT is the severe streaking and cupping artifacts caused by enormous amount of scatter [2], [3]. The potential impact on CBCT images induced by these artifacts mainly lies in two aspects. Firstly, a quantitative inaccuracy of reconstructed CT numbers may be caused, which makes accurate dose-calculation impossible [4]. Secondly, some CBCT-based techniques such as volume visualization and segmentation will be greatly affected [5]. With appropriate artifacts removal approaches, the uniformity of contaminated CBCT images can be improved, which can further contribute to the solutions to the above problems.

Nevertheless, scatter correction is a complex issue. Traditional fan-beam CTs adopting linear array detectors are mainly confronted with 1-D scatter, which is relatively less intensive and can be alleviated by installing collimators. By contrast, the scatter artifacts in CBCT caused by the FPD system are distributed in 2-D form, making the scatter intractable to deal with [6].

Several techniques have been proposed to troubleshoot this problem. These scatter artifacts correction methods can be generally divided into two categories: hardware-based ones and software-based ones.

Hardware-based methods include anti-scatter grid and air gap. However, this type of correction method adds extra hardware to the CBCT system, which can increase its difficulty and complexity [7]. Therefore, efforts are increasingly being directed toward software-based methods, such as Monte Carlo simulation algorithms, scatter estimation methods, partial scattering measurement-based methods and convolutional model-based methods.

In recent years, Monte Carlo (MC) simulation algorithms have been proposed to reduce the scatter artifacts. Examples include the GPU accelerating technology-based method [8] and model-based volume restoration approach [9]. Xu *et al.* [10] proposed an optimized MC simulation approach, which also obtained satisfactory effects. However, it takes at least 3 minutes in conventional MC simulation for a single CBCT projection, which limits its clinical application [11], [12]. The MC method can used the clean CT image to simulate scatter distribution. However, in IGRT system, the CBCT images are contaminated by severe artifacts, for which we are not capable of generating desired scatter distribution.

Most scatter analysis methods are based on the Klein–Nishina formation and Spies' model [13]. Such information as X-ray spectral characteristics, geometrical

structure of the object, and attenuation coefficients is essential to these methods. Yao and Leszczynski [14] acquired an approximate estimation with the above information. Feng *et al.* could estimate the scatter distribution of X-ray irradiated objects in both a homogeneous medium and an inhomogeneous medium. The level set-based method [15] and moving blocker-based method [16] could obtain satisfactory results as well.

Many partial scattering measurement-based methods are available to correct artifact scatters. An early method based on beam stop array (BSA) calculated the overall scattering distribution received by the detector by measuring the amount of scattering under the X-ray blocking array [17]. Then, a normal scan without X-ray blocking array was performed. The scanned projected images were subtracted by the images representing the overall scattering distribution. Ultimately, the corrected images could be acquired. Henceforth, BSA is regarded as an ideal scatter-correction method and has been improved numerous times. Nevertheless, the double scans in this method increased the scanning time and X-ray irradiation dose. Siewerdsen *et al.* [18], Yan *et al.* [19], Ren *et al.* [20], and Lee *et al.* [21] proposed several ways to remove the extra scan. Ouyang *et al.* [22], [23] and Meng *et al.* [24] utilized moving shutters, which could also obtain satisfactory effects without double scans. Zhu *et al.* [25], [26] proposed a primary ray modulation method, with which a modulation board was used to convert the primary ray image of the object into high frequency and then separate the low-frequency component describing the scattering distribution.

Convolutional model-based method, which was adopted by the KV imaging system in the clinical Varian TrueBeam, was proposed early in 1987 by Naimuddin *et al.* [27]. Variants of this method focused on employing different scattering kernel model parameters to implement scatter correction. For instance, Starlack's method [28], [29] could easily tackle the impact of different energy levels of X-ray scattering on CBCT reconstruction images. Flickit was a priori knowledge needed to estimate the scattering kernel model parameters, which, to a certain extent, hindered the range of application and accuracy of this method.

In 2018, Maier *et al.* [30], [31] proposed a deep convolutional neural network (CNN) combined with MC simulations to estimate scatter artifacts. They employed a deep convolutional neural network which was trained to reproduce the output of MC simulations with only projection data as input. In this approach, phantoms instead of real images were used as the prior clean images.

Recently, some generative adversarial network (GAN) based methods have been proposed to directly learn the distribution of groundtruth CT or CBCT images. Zhao *et al.* [32] used Smooth GAN to remove the ring artifacts in CBCT. Wang *et al.* [33] proposed a cGAN-based approach to the correction of the metal artifacts in CT images. These deep learning based approaches used either simulated CBCT images or CT images as groundtruth while training networks. However, it is impossible to obtain clean images (without artifacts) as a priori information for CBCT in an IGRT system.

Inspired by some novel techniques effective in CT denoising [34], the current study proposed a method to handle CBCT artifacts with deep CNN by learning the residuals between contaminated CBCTs and CTs corresponding to the same part of a patient. As CBCT scatter can be quite difficult to estimate accurately, we directly experimented on the raw data obtained from hospitals instead of phantoms. The results presented in section III demonstrate manifest improvements in both cupping and streaking artifacts removal.

This study developed the residual learning of deep CNN and employed it in the scatter artifacts removal of CBCT images in an IGRT system. The flowchart of the proposed feed-forward artifact-free CNN (AFCNN) is shown in Fig. 1.

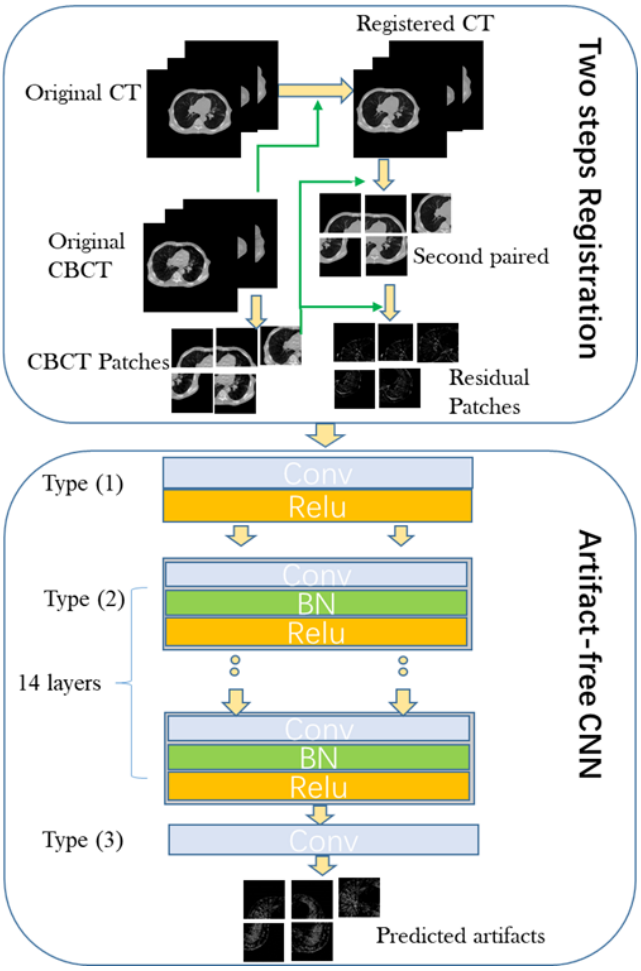


**FIGURE 1.** Flow chart of the proposed method.

The remainder of this paper is organized as follows. In Section II, the AFCNN method for reconstruction is proposed. In Section III, the experimental design and results are reported. Finally, in Section IV, some discussions on the potential applications of corrected CBCTs and conclusions are provided.

## II. METHOD

In this section we will explain the necessity of the registration technique, with which the residual learned by a deep CNN can be ensured to be meaningful enough with only scatter artifacts contained. The proposed method successfully generalizes the residual learning process, which is modeled by a deep network called AFCNN, to CBCT artifacts removal. Relevant details including the network architecture will then be elaborated.

### A. REGISTRATION

Residual learning has been demonstrated to be effective in removing artifacts in CT images. In this work, this approach is developed to learn the mapping from a CBCT image to its corresponding residual image, which shows the difference between this CBCT image and a CT image representing exactly the same scanning position.

Patients receiving radiation therapy are asked to have a CT scan before starting the IGRT. In each radiation therapy, patients must undergo a CBCT scan. Pairs of CBCT–CT can then be acquired from the IGRT system, which make up the dataset we use.

One of the key successes in residual learning is that the residual image (the difference between a training pair) only contains noise and artifacts components and does not contain any meaningful anatomical structures. Hence, we registered CT and CBCT images together before using them as training pairs because registration can minimize structural dissimilarity for a training pair.

Unfortunately, on account of lung breathing, these CBCTs and CTs, though acquired from strictly the same region of the same patient, could be slightly discrepant with respect to position and to detailed information in lung region. In practice, the residual images obtained by CBCTs subtracting CTs are highly dependent on the match pixel by pixel. Therefore, an integral CBCT–CT registration can be important in creating a target set composed of residual images. On top of that, different slice thicknesses between CTs and CBCTs (commonly 2.5 mm or 3.0 mm for CTs and 3.0 mm for CBCTs) result in a disparity in the number of slices even in exactly the same scan interval of a body, which hinders the acquisition of residual images. A voxel-based body registration can tackle this challenge by building a connection between intrinsic coordinates and a world coordinate system, given spatial referencing information that can output a pair of dimension-identical CBCT–CT voxels. In the training phase, mini-block pairs, instead of whole CBCT–registered CT (RCT) pairs, were put into datasets to keep detailed information. Clear discrepancies were still observed between some pairs of mini-blocks; these variations would dramatically impact the training result of the pixel-level-based CNN architecture.

A secondary registration was then applied accordingly to guarantee pixel-by-pixel correspondence. To further ensure the quality of our dataset, we just selected the paired voxels whose maximum normalized cross-correlation coefficient (NCC) surpassed a threshold pre-set as a hyperparameter. As indicated by the experiment result, manifest ghosting at the image boundary was generated without secondary registration, which proved the necessity of this step. Specifically, an image registration method based on mutual information (MI) was adopted to complete these two steps.

In summary, secondary registration tries to eliminate the slight displacements between pixels in CT and CBCT mini-blocks. After the two-step registration, image data are ready to be fed into our deep CNN.

### B. RESIDUAL LEARNING

CNN has shown great success in handling various tasks. In this work, we focused on designing and training a deep CNN architecture effective to learn the residual distribution.

On the basis of the denoising idea in [35], the present work used the residual learning technique for CNNs to learn artifacts of CBCT and then subtracted the artifacts obtained by network from CT images before finally recovering clear correction images.

Inspired by the denoising approach in [36], we combined the residual learning technique with our AFCNN to learn the artifacts of CBCT images. The model we chose is similar to the one used in the general image denoising task, $f = x + n$, except that stands for scatter artifacts. A mapping function $F(f) = n$ should be learned to predict the clean image just as typical denoising models like MLP [37] and CSF [38]. In the current study, we used a deep CNN to learn this mapping from CBCT images with severe scatter artifacts to residuals between CBCT and registered CT images. The mean squared error (MSE) between real and predicted residuals was measured as our object function:

$$l(\Theta) = \frac{1}{2N} \sum_{i=1}^{N} \|\mu(f_i; \Theta) - (f_i - x_i)\|^2 \tag{1}$$

where $\{(f_i, x_i)\}_{i=1}^{N}$ represents N pairs of images that contain artifacts and real images, and $\mu(f)$ is the CNN's mapping function. After the network converges, the residual images can be obtained from the AFCNN, and then the de-artifacts CBCT images can be obtained according to $x = f - n$.

### C. NETWORK STRUCTURE

As is shown in Fig. 1, the network with depth D has three types of layers: (1) convolution network + Rectifier Linear Unit (ReLU), (2) convolution network + batch normalization (BN) + ReLU, and (3) convolution network layer.

In Type (1), 64 filters of size $3 \times 3 \times 1$ are used to generate 64 feature maps. These convolution filters are followed by ReLU, which is an element-level operation (applied to each pixel), setting all pixel values less than 0 in the feature map to 0. The purpose of ReLU is to introduce nonlinearity in the convolution network.

Layers of Type (2) are repeated from the second layer to the D-1 layer with each containing 64 $3 \times 3 \times 64$ filters. BN is added between Convolution and ReLU to improve the convergence speed of the network.

The layer in Type (3) is a convolution layer, which uses filters of size $3 \times 3 \times 64$.

## III. EXPERIMENT

Experiments were conducted on the data acquired from several patients in different hospitals through the IGRT system to verify the proposed method. The results demonstrated that our method can achieve a conspicuous correction effect on both cupping artifacts and streaking artifacts removal. As comparison, we also showed some correction results with Shi's approach in [39].

### A. DATA SET

To acquire real data from IGRT systems, we collected CT and CBCT images from different patients. Specifically, patients were first scanned by CT and then CBCT, thus producing two pairs of slices. Using this method, we acquired 1,225 CT images and 1,093 CBCT images as our dataset. Among these raw data, 352 CBCT slices and 367 CT slices from 5 of 20 patients were separated as the test set. Note that all CT images were $512 \times 512$, while CBCT data consisted of 12 groups of $384 \times 384$ and 8 groups of $512 \times 512$. Each of these raw images was preprocessed with a 3-D registration system, producing 20 groups of CT–CBCT pairs which were cursorily registered. Nevertheless, less than two thousand images can hardly train a deep network from scratch. We therefore split each registered image into several overlapped data patches (each with fixed patch size and stride set as hyper-parameters), which made up our final dataset. The size of the data patches is $80 \times 80$. In this way, we enlarged our dataset to prevent overfitting and forced the network to learn scatter in a more fine-grained manner.

### B. NETWORK TRAINING

The proposed algorithm was trained by an Adam optimizer with the learning rate set from 1e-3 to 1e-5. The number of epochs was set to 50, and the size of the image patch was set to $80 \times 80$ with stride 30.

The network was implemented using the MatConvNet toolbox [40] in a MATLAB 2017a environment, with a GTX 1080 Ti graphic processor, and an i7-6850K CPU (3.60 HZ).

### C. EXPERIMENT RESULTS

Five of 352 experiment results, including CBCT, RCT, CBCT were corrected by the proposed method, and Shi's correction, as is shown in Fig. 2. As DICOM images are commonly int16 format, a HU value window at $[-1000, 700]$ was set for all images to obtain better intuition. Specifically, raw CBCT slices in the first column were prominently contaminated by streaking artifacts, which meant that some detailed information could be destroyed. As is shown in the figure, CBCT slices were smoothly corrected with the proposed method. All noises, including streaking artifacts and cupping artifacts, were clearly removed. Simultaneously, key details such as inner contours and texture information in the lung area were well preserved. By contrast, CBCT processed with Shi's method distinctly improved the quality of slices by correcting cupping artifacts, as is shown in column (d) of Fig. 2 Nevertheless, with respect to the predominant streaking artifacts, Shi's algorithm had a minor impact, which will be further demonstrated.

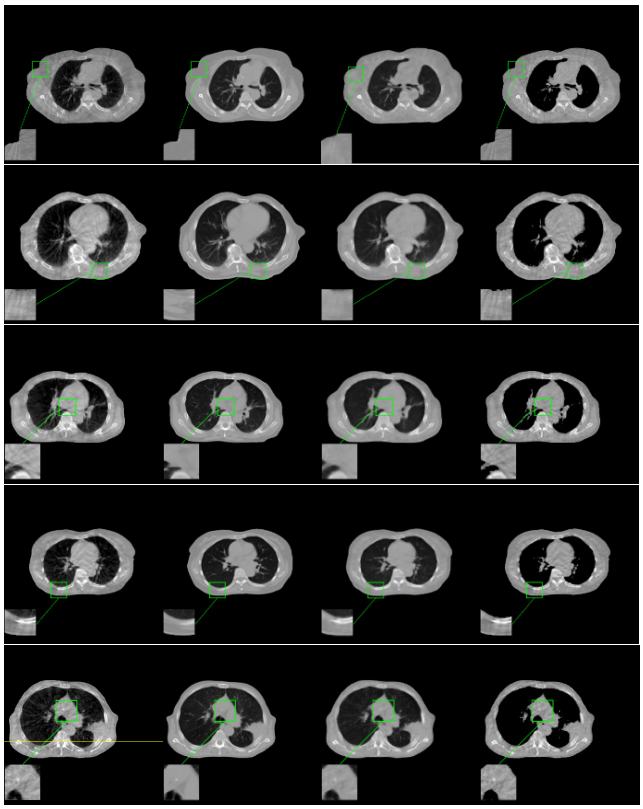


**FIGURE 2.** Scatter correction results on different patients. (a) CBCT. (b) RCT. (c) proposed correction. (d) Shi's correction.

**TABLE 1.** Quantitative analysis Of four slices.

| Measurements | | CBCT | CT | **My_sc** | Shi_sc |
|---|---|---|---|---|---|
| Mean CT numbers (Hu) | Bone | 312.973 | 181.785 | **199.676** | 228.093 |
| | Skin | 87.573 | 28.579 | **27.888** | 32.523 |
| | lungs | -866.357 | -797.877 | **-776.774** | -1019.862 |
| CNR | Bones-Skin | 2.621 | 5.571 | **4.614** | 2.449 |
| Average PSNR | | 7.889 | / | **8.823** | 5.902 |

My_sc and Shi_sc denote our proposed method and Shi's correction method, respectively.

The proposed method takes only 0.0081 second on average for one single prediction, which shows a low time complexity, making it beneficial to further applications.

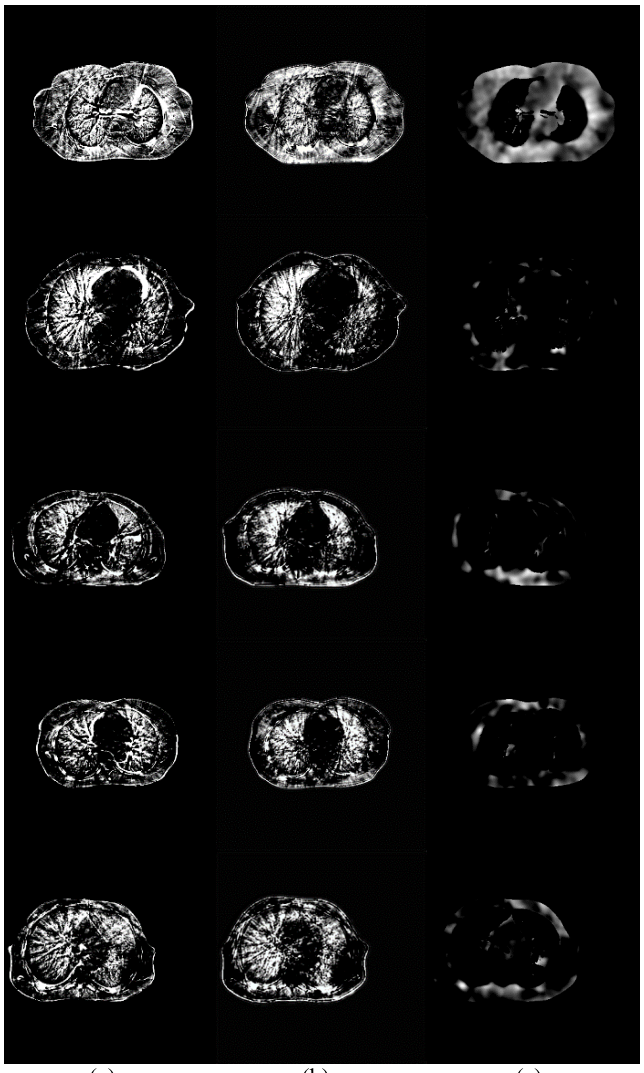


**FIGURE 3.** Residual images. (a) Original residual. (b) Learned residual. (c) Shi's residual.

The quantitative analyses of the four kinds of slices were summarized in Table 1, where My_sc and Shi_sc denote our method and Shi's correction method, respectively. Each of these objective evaluations is the mean of the dada of the five patients. Specifically, CT numbers in Hounsfield units (HU)were calculated in three regions of interest (ROIs), including bone, skin and lungs, to compare the degree of a slice close with the original CT. Compared with Shi's, corrected slices of the proposed method had CT numbers closer to RCT. We also calculated the contrast-to-noise ratio (CNR) using ROIs of bone, skin and lung regions of five patients and averaged them. As is observed, the CNR of CBCT was distinctly improved after being corrected by the proposed method. The average PSNR also supported the result shown above, that is, the artifacts are indeed suppressed through the application of a trained network.

To gain an intuitive sense of what the network had learned exactly, the residual images of five patients between the original CBCT and RCT slices are shown in Fig. 3. Briefly, the trained CNN basically learned how to extract a residual from a given CBCT. Note that the original residual (RCT minus CBCT) image contains not only artifacts but also differences in particular information at lung regions caused by the patient's breath. Shi's correction result, as is shown in the right column, did a great job of eliminating cupping artifacts, while little effects were achieved in suppressing streaking artifacts. A considerable part of the texture was also cleared when correcting scatter at lung regions.

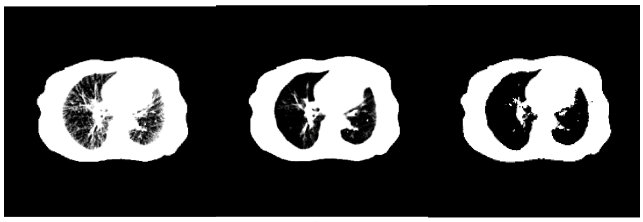


**FIGURE 4.** Corrected thorax regions. (a) CBCT. (b) Proposed method. (c) Shi's methods.

The HU window was adjusted to approximately [-950,500] to obtain a more explicit view of the detailed part of corrected slices. Fig. 4 shows the difference between the proposed method and Shi's method in preserving detail (for conciseness, only one patient's slices were chosen here). As the streaking artifacts in the thorax region could be considerably severe, it was almost impossible to restore texture completely. To a large extent, the proposed method suppressed scatter artifacts and acquired satisfactory results in tumor detection at the least.

## IV. DISCUSSION AND CONCLUSION

The CBCT data acquisition is fundamentally different from the CT data acquisition, at least, the temporal resolution (partially determined by the gantry rotation time) is different. For the same patient who is scanned by both CT and CBCT, the reconstructed images could present different temporal resolutions. To be more specific, CBCT images may present more severe motion artifacts (motion-induced blurring effects) than CT images. Besides, if we applied any respiratory-gated CBCT image reconstruction method, it would still be very difficult to make sure that the paired CBCT images and CT images can represent the same respiratory status of the patient. Hence, it is very difficult to avoid the intrinsic dissimilarity of anatomical structures between CBCT images and CT images. To make sure that residual images truly represent artifacts component with no meaningful anatomical structure contained, a second registration method was applied to reduce the intrinsic dissimilarity of anatomical structures between paired CBCT-CT images.

Then we discarded those pairs whose NCC was below a certain threshold and made the rest ones constitute the final training set. By this means, the alignment of CBCT-CT image pairs is ensured and the size of dataset is expanded.

A representative set of slices was selected to compare the cupping artifacts in the 1D horizontal profiles (y = 235 in

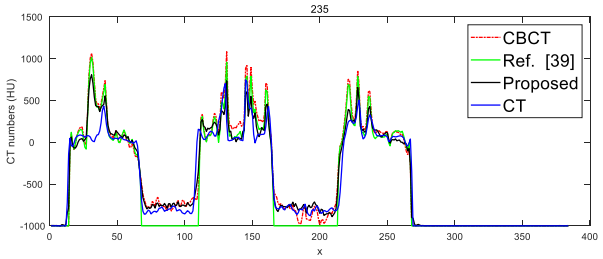


**FIGURE 5.** The 1D horizontal profile of the images which are shown in Fig. 2 (row 5).

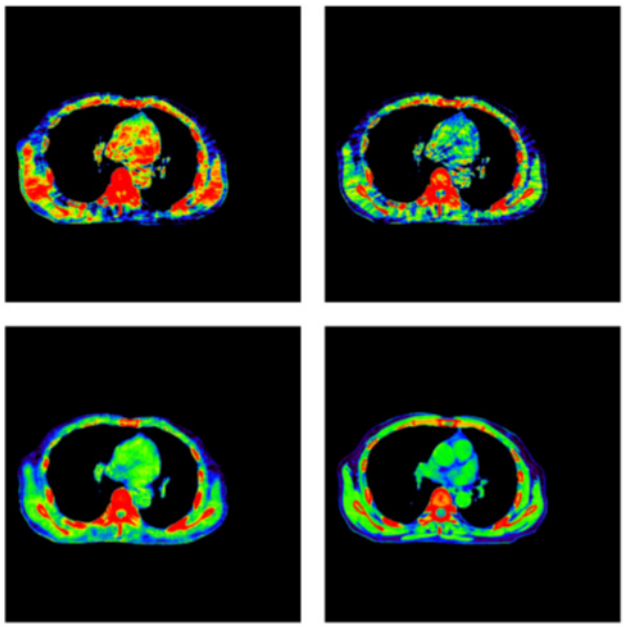

**FIGURE 6.** 2D atlas visualization based on threshold. From top left to bottom right is: CBCT image, Shi's corrected CBCT image, Our corrected CBCT image and CT image. In order to compare the CT numbers with different artifacts removal method, we use 2D atlas to display. Different colors represent different ranges of CT numbers.

Fig. 2 (row 5)). As shown in Fig. 5, the CBCT images corrected by our approach have more uniform distribution of CT numbers along the fixed line than both original and Shi's (closer to the original CT images).

To further illustrate that after removing artifacts with proposed method, the problem described in Section I has been solved to some extent. We visualized the CT numbers-based segmentation effect with the following 4 kinds of slices in Fig. 6. Note that the area marked in red should represent bones. But streaking artifacts with similar CT numbers to bones can easily lead to incorrect segmentation, resulting in the red marked areas shattering everywhere. CBCT corrected by the proposed method shows a segmentation result much closer to CT image.

In this paper, we proposed a learning-based scatter correction method with two-step registration, which was proven to be effective in suppressing scatter artifacts produced by an actual CBCT system. With the use of a deep CNN, the residual between CBCT and RCT can be learned by a model and applied to CBCT from different patients, even from different body parts, as long as corresponding training data are given. Moreover, the proposed method can preserve detailed information, such as texture in thorax regions and inner contours. Therefore, a tiny blur may be introduced to the CBCT slices. Results tested on the data of five patients showed that by using a 17-layer CNN architecture with two-step registration, CNR and average PSNR were significantly improved, and the CT numbers of ROIs also showed evident amelioration. In summary, residual distribution can be well learned and can, therefore, be removed from the contaminated CBCT.

As shown in [41]–[46], there are a lot of style of the CNN. We will research the effect of different networks on scatter artifacts removal.

## ACKNOWLEDGMENT

The authors thank the anonymous referees for their constructive and insightful comments, which greatly improved the presentation of our research results.

## REFERENCES

[1] F. Yang, D. Zhang, K. Huange, W. Shi, and X. Wang, "Scattering estimation for cone-beam ct using local measurement based on compressed sensing," *IEEE Trans. Nucl. Sci.*, vol. 65, no. 3, pp. 941–949, Mar. 2018.
[2] H. Kui-Dong, Z. Hua, S. Yi-Kai, Z. Liang, and X. Zhe, "Scatter correction method for cone-beam CT based on interlacing-slit scan," *Chin. Phys. B*, vol. 23, no. 9, pp. 515–521, Jul. 2014.
[3] H. Zhang, Y. Shi, and K. Huang, "An improved scatter correction method for Cone Beam Computed Tomography," in *Proc. ICSPCC*, Sep. 2011, pp. 1–5.
[4] Y. Takayama *et al.*, "Evaluation of the performance of deformable image registration between planning CT and CBCT images for the pelvic region: Comparison between hybrid and intensity-based DIR," *J. Radiat. Res.*, vol. 58, no. 4, pp. 567–571, 2017.
[5] S. Xie *et al.*, "Artifact removal using improved GoogLeNet for sparse-view CT reconstruction," *Sci. Rep.*, vol. 8, no. 1, Apr. 2018, Art. no. 6700.
[6] B. D. Jo, Y. J. Lee, D. H. Kim, P. H. Jeon, and H. J. Kim, "Scatter correction method with primary modulator for dual energy digital radiography: A preliminary study," *Proc. SPIE*, vol. 9033, p. 90335U, Mar. 2014.
[7] R. Ning, X. Tang, and D. Conover, "X-ray scatter correction algorithm for cone beam CT imaging," *Med. Phys.*, vol. 31, no. 5, pp. 1195–1202, May 2004.
[8] Y. Xu *et al.*, "Ultrafast cone-beam CT scatter correction with GPU-based Monte Carlo simulation," *Med. Phys.*, vol. 2, no. 2, p. 020245, 2014.
[9] G. Zhang, R. Jacobs, and H. Bosmans, "A model-based volume restoration approach for Monte Carlo scatter correction in image reconstruction of cone beam CT with limited field of view," *Phys. Med. Imag.*, vol. 8868, p. 86682P, Mar. 2013.
[10] Y. Xu *et al.*, "A practical cone-beam CT scatter correction method with optimized Monte Carlo simulations for image-guided radiation therapy," *Phys. Med. Biol.*, vol. 60, no. 9, pp. 3567–3587, Apr. 2015.
[11] A. Sisniega *et al.*, "Monte Carlo study of the effects of system geometry and antiscatter grids on cone-beam CT scatter distributions," *Med. Phys.*, vol. 40, no. 5, pp. 1915–2011, 2013.
[12] A. Sisniega *et al.*, "High-fidelity artifact correction for cone-beam CT imaging of the brain," *Phys. Med. Biol.*, vol. 60, no. 4, pp. 1415–1439, Jan. 2015.
[13] L. Spies, P. M. Evans, M. Partridge, V. N. Hansen, and T. Bortfeld, "Direct measurement and analytical modeling of scatter in portal imaging," *Med. Phys.*, vol. 27, no. 3, pp. 462–471, Mar. 2000.
[14] W. Yao and K. W. Leszczynski, "An analytical approach to estimating the first order scatter in heterogeneous medium. II. A practical application," *Med. Phys.*, vol. 36, no. 7, pp. 3157–3167, Jul. 2009.
[15] S. Xie, C. Li, H. Li, and Q. Ge, "A level set method for cupping artifact correction in cone-beam CT," *Med. Phys.*, vol. 42, no. 8, pp. 4888–4895, Aug. 2015.
[16] C. Zhao, L. Ouyang, J. Wang, and M. Jin, "Multi-view scatter estimation for moving blocker scatter correction of CBCT," in *Proc. IEEE Nucl. Sci. Symp., Med. Imag. Conf. Room-Temp. Semicond. Detect. Workshop*, Oct./Nov. 2016, pp. 1–3.

[17] J. S. Maltz *et al.*, "Focused beam-stop array for the measurement of scatter in megavoltage portal and cone beam CT imaging," *Med. Phys.*, vol. 35, no. 6, pp. 2452–2462, 2008.
[18] J. H. Siewerdsen *et al.*, "A simple, direct method for X-ray scatter estimation and correction in digital radiography and cone-beam CT," *Med. Phys.*, vol. 33, no. 1, pp. 187–197, Jan. 2006.
[19] H. Yan, X. Mou, S. Tang, Q. Xu, and M. Zankl, "Projection correlation based view interpolation for cone beam CT: Primary fluence restoration in scatter measurement with a moving beam stop array," *Phys. Med. Biol.*, vol. 55, no. 21, pp. 6353–6375, Nov. 2011.
[20] L. Ren, F.-F. Yin, I. J. Chetty, D. A. Jaffray, and J.-Y. Jin, "Feasibility study of a synchronized-moving-grid (SMOG) system to improve image quality in cone-beam computed tomography (CBCT)," *Med. Phys.*, vol. 39, no. 8, pp. 5099–5110, Aug. 2012.
[21] H. Lee, L. Xing, R. Lee, and B. P. Fahimian, "Scatter correction in cone-beam CT via a half beam blocker technique allowing simultaneous acquisition of scatter and image information," *Med. Phys.*, vol. 39, no. 5, pp. 2386–2395, May 2012.
[22] L. Ouyang, K. Song, and J. Wang, "A moving blocker system for cone-beam computed tomography scatter correction," *Med. Phys.*, vol. 40, no. 7, p. 071903, Jul. 2013.
[23] X. Chen *et al.*, "Optimization of the geometry and speed of a moving blocker system for cone-beam computed tomography scatter correction," *Med. Phys.*, vol. 44, no. 9, pp. 215–229, Sep. 2017.
[24] B. Meng, H. Lee, L. Xing, and B. P. Fahimian, "Single-scan patient-specific scatter correction in computed tomography using peripheral detection of scatter and compressed sensing scatter retrieval," *Med. Phys.*, vol. 40, no. 1, p. 011907, Jan. 2013.
[25] L. Zhu, Y. Xie, J. Wang, and L. Xing, "Scatter correction for cone-beam CT in radiation therapy," *Med. Phys.*, vol. 36, no. 6, pp. 2258–2268, Jun. 2009.
[26] L. Zhu, J. Wang, and L. Xing, "Noise suppression in scatter correction for cone-beam CT," *Med. Phys.*, vol. 36, no. 3, pp. 741–752, Mar. 2009.
[27] S. Naimuddin, B. Hasegawa, C. A. Mistretta, "Scatter-glare correction using a convolution algorithm with variable weighting," *Med. Phys.*, vol. 14, no. 3, pp. 330–334, May 1987.
[28] J. Star-Lack and M. Sun, "Scatter correction with kernel perturbation," *Proc. SPIE*, vol. 8668, pp. 86681I-1–86681I-8, Mar. 2013.
[29] A. Wang *et al.*, "Asymmetric scatter kernels for software-based scatter correction of gridless mammography," *Proc. SPIE*, vol. 9412, p. 94121I, Mar. 2015.
[30] J. Maier, Y. Berker, S. Sawall, and M. Kachelrieÿ, "Deep scatter estimation (DSE): Feasibility of using a deep convolutional neural network for real-time X-ray scatter prediction in cone-beam CT," *Phys. Med. Imag.*, vol. 10573, p. 105731L, Mar. 2018.
[31] J. Maier, S. Sawall, M. Knaup, and M. Kachelrieß, "Deep scatter estimation (DSE): Accurate real-time scatter estimation for X-ray CT using a deep convolutional neural network," *J. Nondestruct. Eval.*, vol. 37, no. 3, p. 57, Sep. 2018.
[32] S. Zhao, J. Li, and Q. Huo, "Removing ring artifacts in CBCT images via generative adversarial network," in *Proc. ICASSP*, Apr. 2018, pp. 1055–1059.
[33] J. Wang, Y. Zhao, J. H. Noble, and B. M. Dawant, "Conditional generative adversarial networks for metal artifact reduction in CT images of the ear," in *Proc. MICCAI*, Granada, Spain, vol. 11070, Sep. 2018, pp. 3–11.
[34] A. Wang *et al.*, "Asymmetric scatter kernels for software-based scatter correction of gridless mammography," *Proc. SPIE*, vol. 9412, p. 94121I, Mar. 2015.
[35] Y. S. Han, J. Yoo, and J. C. Ye. (2016). "Deep residual learning for compressed sensing CT reconstruction via persistent homology analysis." [Online]. Available: https://arxiv.org/abs/1611.06391
[36] K. Zhang, W. Zuo, Y. Chen, D. Meng, and L. Zhang, "Beyond a Gaussian denoiser: Residual learning of deep CNN for image denoising," *IEEE Trans. Image Process.*, vol. 26, no. 7, pp. 3142–3155, Jul. 2017.
[37] H. C. Burger, C. J. Schuler, and S. Harmeling, "Image denoising: Can plain neural networks compete with BM3D?" in *Proc. IEEE Conf. Comput. Vis. Pattern Recognit.*, Jun. 2012, pp. 2392–2399.
[38] U. Schmidt and S. Roth, "Shrinkage fields for effective image restoration," in *Proc. IEEE Conf. Comput. Vis. Pattern Recognit.*, Jun. 2014, pp. 2774–2781.
[39] L. Shi, T. Tsui, J. Wei, and L. Zhu, "Fast shading correction for cone beam CT in radiation therapy via sparse sampling on planning CT," *Med. Phys.*, vol. 44, no. 5, pp. 1796–1808, May 2017.
[40] A. Vedaldi and K. Lenc, "MatConvNet: Convolutional neural networks for matlab," in *Proc. 23rd ACM Int. Conf. Multimedia*, 2015, pp. 689–692.
[41] S.-H. Wang, J. Sun, P. Phillips, G. Zhao, and Y.-D. Zhang, "Polarimetric synthetic aperture radar image segmentation by convolutional neural network using graphical processing units," *J. Real-Time Image Process.*, vol. 15, no. 3, pp. 631–642, 2018.
[42] S.-H. Wang *et al.*, "Multiple sclerosis identification by 14-layer convolutional neural network with batch normalization, dropout, and stochastic pooling," *Frontiers Neurosci.*, vol. 12, Nov. 2018, Art. no. 818.
[43] Y.-D. Zhang, C. Pan, J. Sun, and C. Tang, "Multiple sclerosis identification by convolutional neural network with dropout and parametric ReLU," *J. Comput. Sci.*, vol. 28, pp. 1–10, Sep. 2018.
[44] Y.-D. Zhang, C. Pan, X. Chen, and F. Wang, "Abnormal breast identification by nine-layer convolutional neural network with parametric rectified linear unit and rank-based stochastic pooling," *J. Comput. Sci.*, vol. 27, pp. 57–68, Jul. 2018.
[45] Y.-D. Zhang, K. Muhammad, and C. Tang, "Twelve-layer deep convolutional neural network with stochastic pooling for tea category classification on GPU platform," *Multimedia Tools Appl.*, vol. 77, no. 17, pp. 22821–22839, 2018.
[46] S.-H. Wang, Y.-D. Lv, Y. Sui, S. Liu, S.-J. Wang, and Y.-D. Zhang, "Alcoholism detection by data augmentation and convolutional neural network with stochastic pooling," *J. Med. Syst.*, vol. 42, no. 1, Jan. 2018, Art. no. 2.

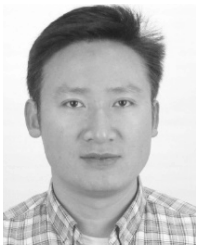

**SHIPENG XIE** received the B.S. degree in mathematical sciences from Anhui University in 2003, and the Ph.D. degree in computer science and engineering from Southeast University, Nanjing, China, in 2012. From 2006 to 2013, he served as an Officer in Anhui University. In 2013, he joined the Nanjing University of Posts and Telecommunications as an Assistant Professor, where he is currently an Associate Professor in computational imaging and computer vision harnessing both variational and learning-based methods.

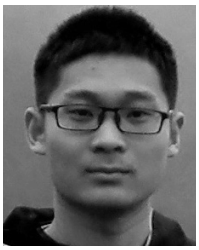

**CHENGYUAN YANG** received the B.S. degree from the Nanjing University of Posts and Telecommunications, where he is currently pursuing the master's degree with a focus on the research of medical imaging.

**ZIJIAN ZHANG** received the B.S. degree in nuclear engineering and nuclear technology from the University of South China, China. He completed his Medical Physicist Residency at Xiangya Hospital Central South University, Changsha, China, where he is a Superior Medical Physicist. He is a member of the Large-scale Image Aggregation for Machine learning/Big Data Application which is launched by MD Anderson. Currently, he is responsible for processing data in the Asian region.

**HAIBO LI** is currently a Professor in computational imaging and computer vision with the Nanjing University of Posts and Telecommunications.